JACS
JOURNAL OF THE AMERICAN CHEMICAL SOCIETY

ARTICLE

pubs.acs.org/JACS

# Synthesis and Characterization of $Au_{102}(p\text{-MBA})_{44}$ Nanoparticles

Yael Levi-Kalisman,[†] Pablo D. Jadzinsky,[†] Nir Kalisman,[†] Hironori Tsunoyama,[‡] Tatsuya Tsukuda,[‡] David A. Bushnell,[†] and Roger D. Kornberg*[,†]

[†]Department of Structural Biology, Stanford University School of Medicine, Stanford, California 94305, United States

[‡]Section of Catalytic Assemblies, Catalysis Research Center, Hokkaido University, Sapporo 001-0021, Japan

Supporting Information

**ABSTRACT:** The synthesis of $Au_{102}(p\text{-MBA})_{44}$ nanoparticles on a preparative scale in high yield is described. Various analytical methods are shown to give results consistent with the composition and known structure of the particles, showing the preparation is essentially homogeneous, and attesting to the validity of the methods as well. Derivatization of the particles with proteins and DNA is demonstrated, and conditions are described for imaging individual particles by cryo-EM at low electron dose, close to focus, conditions optimal for recording high-resolution details.

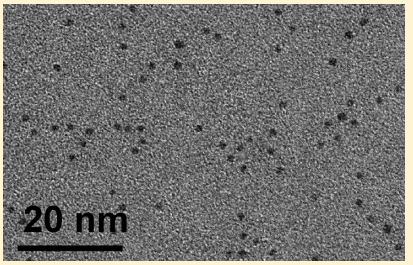


## INTRODUCTION

Development of a facile synthesis of nanometer-size gold particles, stabilized by thiolate monolayers, opened the way to fundamental studies and potential applications.[1,2] The particles were initially heterogeneous in size, and the question arose whether a homogeneous preparation could be obtained, or whether exchange of gold atoms between particles would preclude the possibility. The answer came from the production of particles so uniform in size that they could be crystallized.[3] X-ray crystal structure determination at 1.1 Å resolution revealed a cluster of 102 gold atoms surrounded by 44 *p*-mercaptobenzoic acid (*p*-MBA) ligands.[4]

The X-ray structure of $Au_{102}(p\text{-MBA})_{44}$ was informative in two further regards. First, it led to calculations by density functional theory showing that the composition and structure of the $Au_{102}$ compound reflect the closure of an electronic shell.[5] The entire gold cluster behaves as a superatom, with stable states corresponding to noble gas electronic configurations. Second, the X-ray structure revealed the nature of the Au−S interface, which may be described as an $Au_{23}(p\text{-MBA})_{44}$ layer protecting a central $Au_{79}$ core.

Nanometer-size gold cluster compounds have previously been characterized with respect to composition and structure by various techniques, including mass spectrometry,[6,7] NMR,[8,9] thermogravimetric analysis,[10,11] optical absorption,[9] electrochemistry,[12,13] electron microscopy,[11,14] X-ray photoelectron spectroscopy,[11,15] and powder X-ray diffraction.[9] Here, we investigate the information gained from these techniques by their application to the $Au_{102}(p\text{-MBA})_{44}$ compound. An initial obstacle was the preparation of the compound. It was first crystallized for X-ray structure determination from a mixture in which it was present in a trace amount. We have now developed an improved procedure that yields the compound in abundant, essentially pure form.

Most applications of gold nanoparticles require the attachment of additional molecules. We previously described the exchange of *p*-MBA ligands on presumptive $Au_{144}$ particles for other sulfhydryl compounds, including proteins and suitably modified nucleic acids.[3,16,17] We further showed that exchange could be limited to a single protein by the replacement of all remaining *p*-MBA ligands with glutathione. We report here on the implementation of these procedures for $Au_{102}(p\text{-MBA})_{44}$. An application of particular concern to us is the labeling of biological objects for structure determination by cryo-electron microscopy.[18] To this end, we have reacted the $Au_{102}$ compound with single chain antibody fragments (scFvs) directed against biological objects of interest. The gold particles must then be visible in images recorded under low dose conditions, close to focus, conditions appropriate for recording high-resolution details. We demonstrate here the feasibility of $Au_{102}$ for this purpose and conditions for imaging the particle in this way.

## EXPERIMENTAL SECTION

**Synthesis.** Aqueous solutions of 95 mM *p*-MBA (TCI America), 300 mM NaOH, and 28 mM $HAuCl_4$ [Gold(III) chlorate trihydrate, Sigma-Aldrich] are combined with water and methanol to give 3 mM $HAuCl_4$, 9 mM *p*-MBA, and 47% (v/v) methanol. The mixture (12 mL in a 50 mL Falcon tube) is kept for 1 h at room temperature on a rocking platform. A freshly prepared solution of 150 mM $NaBH_4$ in water is added to the Au/*p*-MBA mixture in a 2:1 ratio of $NaBH_4$:Au, and rocking is continued at room temperature from a minimum of 5 h to as long as overnight. Following the $NaBH_4$ addition, the mixture turns black, indicative of the gold cluster formation. The product is precipitated by the

**Received:** October 11, 2010
**Published:** February 14, 2011





dx.doi.org/10.1021/ja109131w | *J. Am. Chem. Soc.* 2011, 133, 2976–2982

addition of ammonium acetate (to 80 mM) or NaCl (to 10 mM) and methanol (to 80%) and collected in a microfuge at 13 000*g* for 10 min. The pellet is allowed to dry in air overnight, redissolved in 200 $\mu$L of water, and purified by fractional precipitation (removal of contaminant precipitating at 60% methanol − pellet "0"). To this end, the solution is adjusted to 0.12 M ammonium acetate, 60% methanol, and centrifuged at 13 000*g* for 10 min. The supernatant (supernatant "0") is centrifuged repeatedly until no further precipitate is formed, adjusted to 0.12 M ammonium acetate, 80% methanol, and centrifuged (gives pellet "1"). The pellet from precipitation at 60% methanol (pellet "0") is re-extracted for improved yield, by dissolving in water and precipitating at 60% methanol as before, followed by precipitation of the product from the supernatant (supernatant "1") at 80% methanol as above (gives pellet "2"). The two pellets ("1", "2") from precipitation at 80% methanol are dissolved in a minimum volume of water and combined. The pH of these products is about 6.

**Crystallization.** Crystals were grown in a solution containing 100 mM sodium acetate (pH of the sodium acetate solution was adjusted to 2.5), 300 mM sodium chloride, and 48% methanol. For visualization by scanning electron microscopy (SEM), drops containing crystals were mounted on a SEM aluminum stub (with or without double-sided carbon tape) and left to dry. Images of the crystals were obtained with a Hitachi S-3400N SEM at 15 kV using the BSE detector.

**Mass Spectrometry.** Electrospray ionization (ESI) mass spectra of nanoparticles were obtained on a homemade TOF mass spectrometer.[15] Electrospray was performed with nanoparticles (1.0 mg/mL) in 50% (v/v) methanol/water at a flow rate of 1 $\mu$L/min through a stainless steel needle biased at about −3 kV. The charged liquid droplets were fed into a capillary, which was resistively heated to about 180 °C, forming intact nanoparticle ions by desolvation. The ESI mass spectra were calibrated by reference to those of $Na_nI_{n+1}^-$ cluster anions recorded under the same condition. The spectra presented here were taken without the reflectron, and the typical resolution is about 400 m/Dm.

For MALDI-TOF MS, an aqueous solution of $Au_{102}(p\text{-MBA})_{44}$ (0.1 mg/10 $\mu$L) was mixed with an equal volume of methanolic solution of *trans*-2-[3-(4-tert-butylphenyl)-2-methyl-2-propenylidene] malononitrile (DCTB; 0.1 mg/10 $\mu$L; molar ratio of DCTB/$Au_{102}(p\text{-MBA})_{44}$ ~100). The mixture was cast on a stainless steel plate and dried in air for 1 h. MALDI mass spectra were recorded with a time-of-flight mass spectrometer (Applied Biosystems, Voyager-DE STR-H) operated with a $N_2$ laser (337 nm, 3 Hz, <100 $\mu$J) in the positive ion mode with delayed extraction.

**TGA.** Thermal gravimetric analyses were performed with the use of a Mettler Toledo TGA/SDTA 851 under a nitrogen flow of 20 mL/min. TGA runs of dried samples (dried overnight in a vacuum oven at 90 °C before analysis) in aluminum crucibles were recorded at a heating rate of 10 °C/min in a temperature range of 25−600 °C.

**XPS.** X-ray photoelectron spectrometry was performed with a PHI 5000 VersaProbe scanning ESCA microprobe (Physical Electronics, Chanhassen, MN) equipped with an Al (Kα) X-ray radiation source (1486.6 eV, 46W). Spot size was about 200 $\mu$m. Nanoparticles were dried and mounted as a powder on a metal holder with double-sided tape.

**Electron Microscopy.** Imaging was performed with an FEI G2 F20 field-emission microscope operated at an acceleration voltage of 200 kV, and images were recorded on a 4K × 4K CCD camera (Gatan US4000). For transmission EM, 3 $\mu$L of nanoparticles (0.1−0.5 mg/mL) was applied to glow discharged grids [carbon support film on 400 mesh copper specimen grids (EMS)] that had been pretreated with 0.1% w/v poly L-lysine in water. The excess liquid was blotted with a filter paper, and the grids were allowed to dry in air. Images were collected at a magnification of 200 000×.

For cryo-EM, 3 $\mu$L of nanoparticles (about 1 mg/mL in 0.1 M sodium phosphate buffer, pH 8, to avoid aggregation) was applied to a glow discharged, 200 mesh, lacey carbon copper grid (SPI supplies). To some grids, 4 uL of 10 nm colloidal gold (SPI Supplies) was applied and blotted before application of $Au_{102}(p\text{-MBA})_{44}$, to serve as fiducial markers and facilitate the registration of serial images (see below). Vitrification was performed with a Vitrobot Mark V (FEI), and vitrified samples were transferred to a cryo-holder (Gatan model 626) and examined below −170 °C. Focal series were recorded at a magnification of 80 000× under low dose conditions (15−20 electrons/Å$^2$), on different days with different grids in different orders of defocus values (from focus to 1600 nm defocus and the reverse).

**Image Analysis.** Average nanoparticle images, noise levels, and SNR values at different defocus values were computed for each focal series. Within each series, about 200 nanoparticle locations were manually marked on the 800 nm defocus micrograph. The nanoparticles chosen were well separated and free of any aggregation. There were two computational challenges: how to transfer the marked positions from the 800 nm defocus micrograph to the rest of the micrographs in the series, and how to find the true centers of the nanoparticles. The transfer of marks between micrographs proceeded in two steps. The first was coarse registration of the micrographs in the series by alignment of the centers of 10 nm colloidal gold particles, visible at any defocus value. We noted at a later stage of the work that prominent features on the carbon edge were effective for coarse registration, making the 10 nm colloidal gold unnecessary. The coarse registration allowed the transfer of any mark to within 10 pixels (1 pixel = 1.45 Å) of the nanoparticle center in another micrograph. A better localization of the nanoparticle center was then achieved by a local cross-correlation search between the micrograph and a theoretical mask of the nanoparticle. These local searches amounted to 200 vectors of estimated movement of each mark between the two micrographs. A least-squares linear fit of the noisy 200 vectors gave a transformation that fully compensated for drift and magnification changes occurring between micrographs. We estimate that the final fine registration was accurate to less than 2 pixels. After the fine registration was completed, we sought a better estimate for each nanoparticle center than the original manual mark. To that end, we transferred each mark from the 800 nm micrograph to the other micrographs using the fine registration. In each of the micrographs and for each of the marks, we performed a local cross-correlation search between the micrograph and a theoretical mask of the nanoparticle. This resulted in a calculated nanoparticle center that varied slightly between micrographs. We chose the four micrographs with the best consensus of the nanoparticle center and averaged the four positions. This averaged position replaced the manual mark for the nanoparticle center.

Average nanoparticle images were obtained by averaging of image crops of 40 × 40 pixels around the processed nanoparticle marks from each micrograph. Background statistics at each defocus value were obtained by manually marking about 200 vacant positions in the 800 nm micrograph and transferring them between micrographs using the fine registration transform. Care was taken to mark vacant position in area adjacent to where the marked nanoparticles were, but at least 30 pixels away from any visible nanoparticle. Noise statistics were computed from the gray-level distributions of all the individual pixels in image crops of 40 × 40 pixels around the processed background marks. Assuming that the gray-level values in the background locations follow a normal distribution, the noise was defined as the standard deviation of this distribution. The noise levels at the various defocus values turned out to be nearly the same.

The radial projection of the crystallographic structure of $Au_{102}(p\text{-MBA})_{44}$[4] was calculated by averaging the cumulative *Z*-number through 1000 randomly oriented cross sections. Only the gold ($Z = 79$) and the sulfur ($Z = 16$) atoms of the crystal structure were considered. Image processing was done in MATLAB and was facilitated by the MATLAB GUI tools.

**Bioconjugation.** A scFv directed against RNA polymerase II, modified with a cysteine residue at the N-terminus (1.3 mg/mL), was

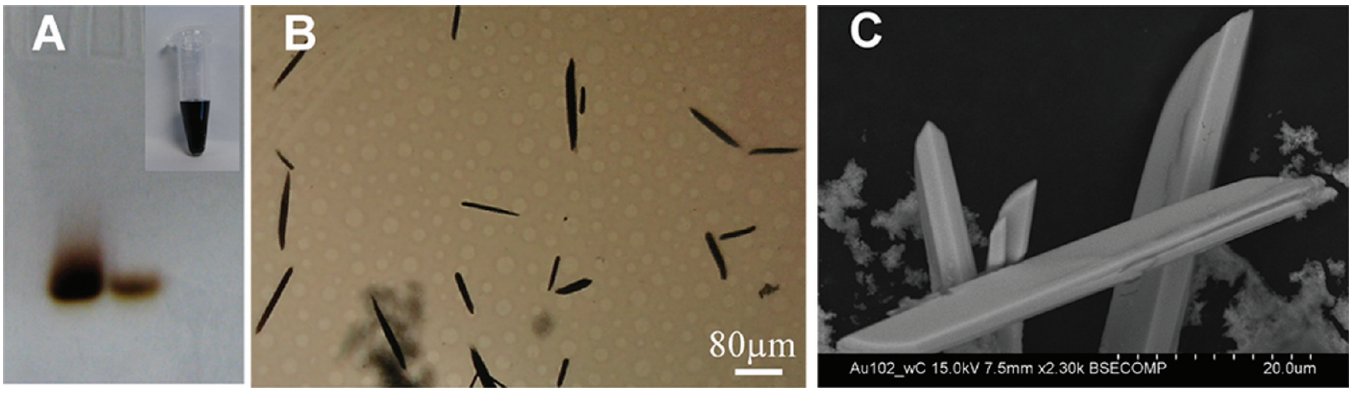


**Figure 1.** Analysis of reaction product by 20% PAGE gel (A) before (left lane) and after (right lane) purification by fractional precipitation. Inset: The reaction product. Crystals of $Au_{102}(p\text{-MBA})_{44}$ imaged by light microscopy (B) and scanning electron microscopy (C).

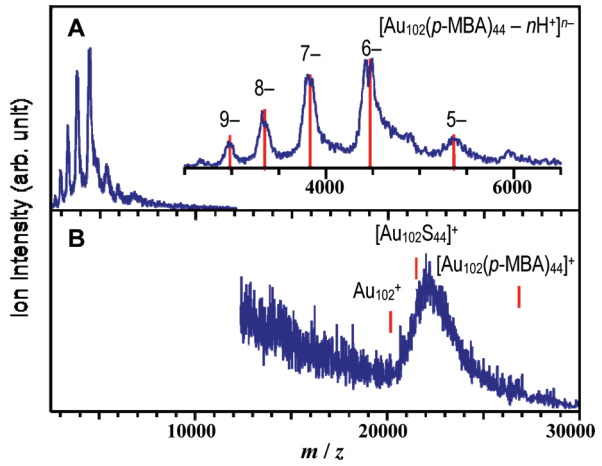


**Figure 2.** ESI (A) and MALDI-TOF (B) mass spectra of the gold clusters. The red bars in panel A indicate calculated peak positions for $[Au_{102}(p\text{-MBA})_{44} - nH^+]^{n-}$.

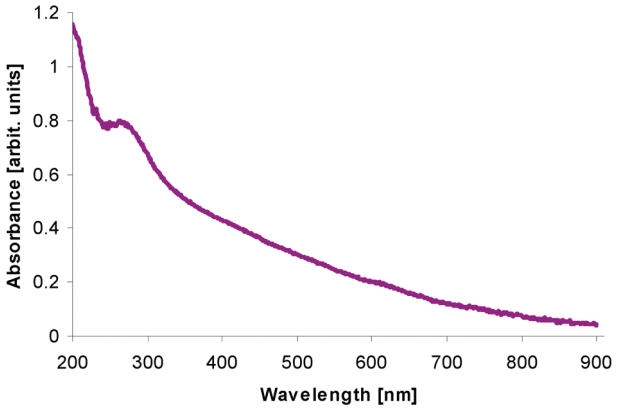


**Figure 3.** UV−visible spectrum of purified $Au_{102}$ preparation ($2 \times 10^{-6}$ M).

reduced with 2 mM tris(2-carboxyethyl)phosphine (TCEP) for 1 h at 37 °C. $Au_{102}(p\text{-MBA})_{44}$ (2 μL of 20 mg/mL) was added to 6 μL of the reduced scFv (2 μL of water was added to 6 μL of reduced scFv as a control) and allowed to react for 1 h at 37 °C.

The oligodeoxyribonucleotide 5′-CTGCTTATCGGTAG/3ThioMC3-D/-3′, synthesized by Integrated DNA Technologies (40 μL of 0.5 mM), was reduced by treatment with 2 mM TCEP for 1 h at 37 °C. $Au_{102}(p\text{-MBA})_{44}$ (2 μL of 20 mg/mL) was added to 8 μL of the reduced oligonucleotide (at 0.5, 0.25, and 0.08 mM) and allowed to react for 1 h at 37 °C.

Repassivation was performed by reacting equal volumes of 20 mg/mL $Au_{102}(p\text{-MBA})_{44}$ and glutathione (100 mM final concentration) for 1 h at 37 °C. Excess glutathione was removed by precipitation with ammonium acetate and methanol, as described above, and resuspension in water.

## RESULTS AND DISCUSSION

**Preparation of $Au_{102}(p\text{-MBA})_{44}$.** Following the method of Brust et al.,[19] the synthesis of $Au_{102}(p\text{-MBA})_{44}$ is performed in two steps: *p*-MBA and $HAuCl_4$ (3:1 ratio of *p*-MBA:gold) are combined in water and 47% methanol at a final gold concentration of 3 mM; $NaBH_4$ is added (2:1 ratio of $BH_4^-$:gold), and the reaction is allowed to proceed from a minimum of 5 h to as long as overnight at room temperature. The product is purified by fractional precipitation with methanol. PAGE gave a single band (Figure 1A) of the same mobility as observed for $Au_{102}(p\text{-MBA})_{44}$ in the past.[4] Crystallization led to the growth of large black rods, a few micrometers in width and few tens of micrometers in length (Figure 1B,C), which gave X-ray diffraction identical to that obtained from $Au_{102}(p\text{-MBA})_{44}$ in the past. The yield was 50−70% (conversion of Au from $HAuCl_4$ to $Au_{102}(p\text{-MBA})_{44}$). The product was stable in aqueous solution at 4 °C for at least 6 months and could be dried and resuspended at will.

**Mass Spectrometry (MS).** Electro-spray ionization (ESI) MS has been used to determine the chemical formulas and charge states of thiolate-protected gold clusters.[7] Application of ESI MS to our purified $Au_{102}$ preparation gave a series of peaks with mass to charge ratios corresponding to partially deprotonated states of $Au_{102}(p\text{-MBA})_{44}$ (Figure 2A). The breadth of the peaks could reflect slight contamination by particles of different compositions, such as $Au_{101}(p\text{-MBA})_{43}$, $Au_{102}(p\text{-MBA})_{42}$, etc.

MALDI-TOF MS employs laser irradiation for vaporization and ionization, resulting in C−S bond breakage. Application to our purified $Au_{102}$ preparation gave a broad peak centered at ∼22 kDa (Figure 2B), consistent with 102 gold atoms and 44 sulfur atoms.

**UV−vis Spectroscopy.** The UV−visible absorption spectrum of the purified $Au_{102}$ preparation decays toward the visible (Figure 3). Except for a peak at 269 nm, attributable to *p*-MBA, the spectrum is featureless. The lack of a surface plasmon resonance band is consistent with previous studies of sub-2 nm gold clusters.[2,20] Linear regression of the plot of absorbance at 520 nm


dx.doi.org/10.1021/ja109131w | J. Am. Chem. Soc. 2011, 133, 2976–2982

versus concentration gave a molar extinction coefficient of $2.33 \times 10^5$ L/mol·cm ($\pm 0.05 \times 10^5$) (Figure S1), consistent with previous estimates of about $4 \times 10^5$ L/mol·cm for monolayer-protected gold clusters of similar dimensions.[21−23]

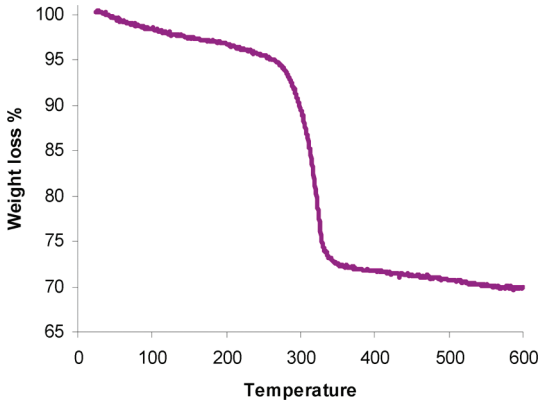


**Figure 4.** Thermogravimetric analysis of purified $Au_{102}$ preparation.

**Thermogravimetric Analysis (TGA).** Weight loss upon heating is commonly used to estimate the percentage of organic material in monolayer-protected gold clusters.[11,24] Heating of our purified $Au_{102}$ preparation resulted in a major decrease in mass between 260 and 360 °C, corresponding to 23% weight loss, and a total loss of 30.2% in the full range from 25 to 600 °C (Figure 4). Two repetitions of the analysis gave 23.2% major weight loss and 31.9% total loss, and 21.4% major weight loss and 29.1% total loss. A value of 25.2% is expected for $Au_{102}(p\text{-MBA})_{44}$. The discrepancy may reflect some importance of the weight loss before and after the major decrease, contamination by particles of other compositions, or inaccuracy of the procedure.

The purified $Au_{102}$ preparation that was subjected to TGA had been precipitated with methanol in the presence of ammonium acetate, and was therefore in a fully protonated state, or rapidly converted from the ammonium ion salt to this state upon heating. At the end of the TGA procedure, after the organic

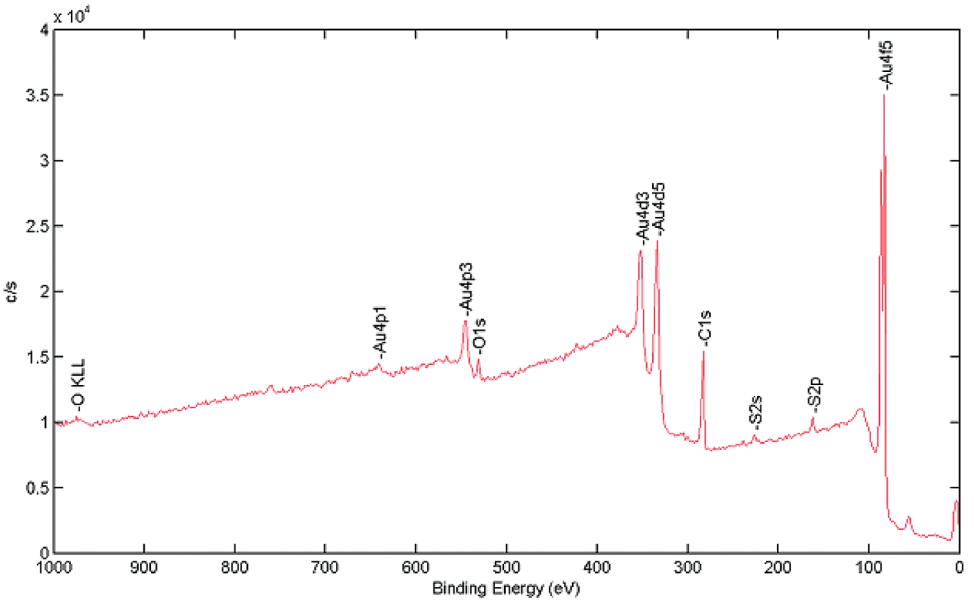


**Figure 5.** XPS survey spectrum of purified $Au_{102}$ preparation.

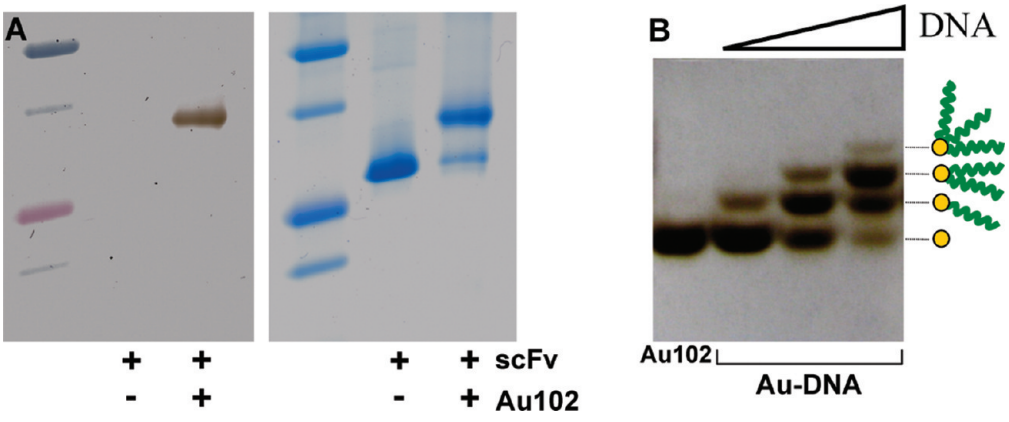


**Figure 6.** Bioconjugation of purified $Au_{102}$ preparation. (A) Reaction with scFv revealed by SDS 12% PAGE, unstained (left panel) or stained with Coomassie blue (right panel). Left lane, Precision Plus Protein standards; middle lane, scFv; right lane, reaction product. (B) Reaction with oligodeoxyribonucleotide revealed by 20% PAGE in TBE. Left lane, $Au_{102}$ preparation. Right three lanes, reaction product with increasing oligodeoxyribonucletide (DNA) concentration (0.08, 0.25, 0.5 mM).


dx.doi.org/10.1021/ja109131w |J. Am. Chem. Soc. 2011, 133, 2976–2982

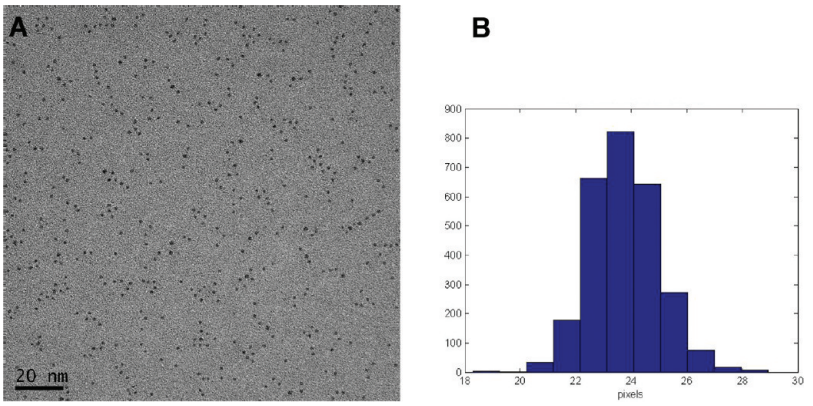


**Figure 7.** (A) Transmission electron micrograph of purified $Au_{102}$ preparation (200 000×). (B) Histogram of numbers of particles (ordinate) with diameters in pixels (abscissa, 1 pixel = 0.56 Å).

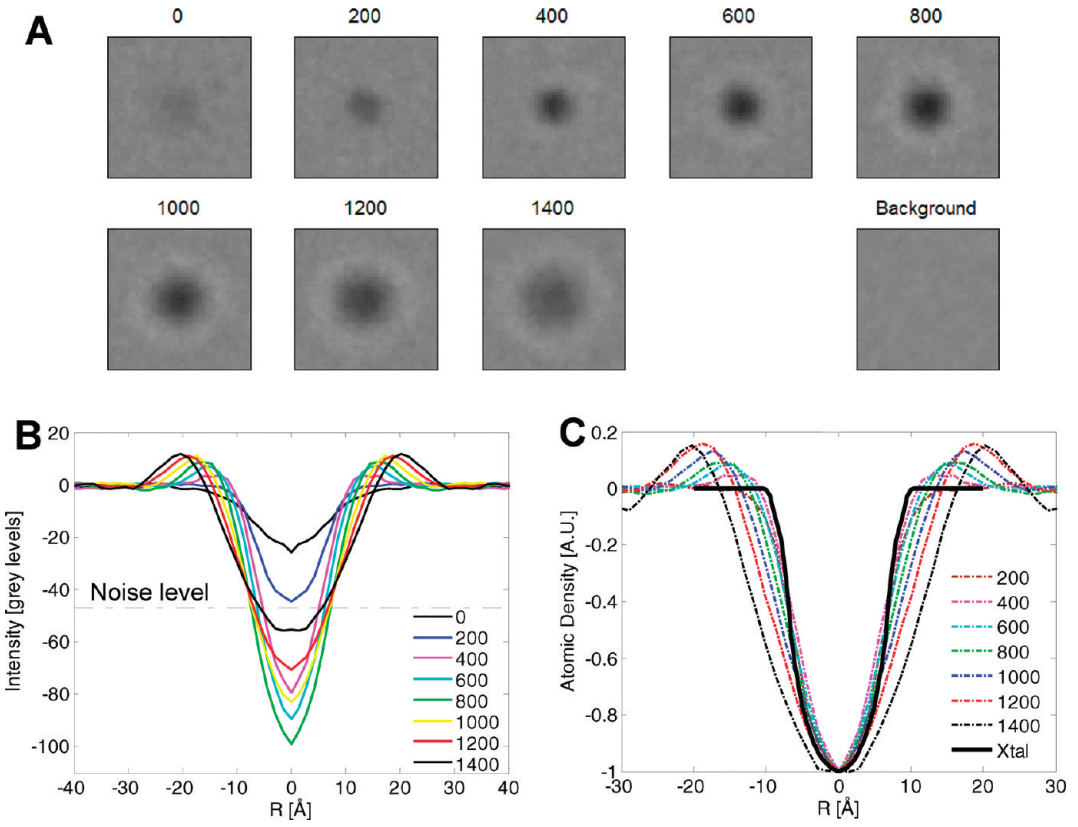


**Figure 8.** (A) Average particle images at defocus values indicated (in nm). (B) Radial intensity distributions of average particle images. (C) Projected radial density distribution computed from crystal structure of $Au_{102}(p\text{-MBA})_{44}$ (Xtal) as compared to normalized radial intensity distributions of average particle images.

material was vaporized, a shiny gold residue remained in the crucible. Purified $Au_{102}$ preparation precipitated with methanol in the presence of NaCl gave aberrant results, presumably because of significant $Na^+$ rather than $H^+$ counterions, and the residue following TGA was black.

**X-ray Photoelectron Spectrometry (XPS).** All the expected atoms, Au, S, C, and O, were revealed by an XPS survey spectrum of the purified $Au_{102}$ preparation (Figure 5). C and O were neglected due to possible contributions from the double-sided tape on which the sample was mounted. Integration of $Au_{4f}$ and $S_{2p}$ peak intensities in high-sensitivity scans (peak positions at 82.7 and 162.1 eV) gave 72.8% Au and 27.2% S. The values calculated for $Au_{102}(p\text{-MBA})_{44}$ are 69.9% Au and 30.1% S.

**Reactivity toward Biomaterials.** The reactivity of a presumptive $Au_{144}$ gold particle with a *p*-MBA surface layer toward protein or DNA sulfhydryl groups was previously demonstrated.[3] Conjugation of a single protein or DNA per particle was accomplished by use of the particles in large excess. Conjugation of additional proteins could be prevented by replacement of *p*-MBA with glutathione, shown previously to produce a less reactive surface layer.[17] It was unclear whether the $Au_{102}(p\text{-MBA})_{44}$ particle would display a similar reactivity profile. The rigidity of


dx.doi.org/10.1021/ja109131w | *J. Am. Chem. Soc.* 2011, 133, 2976–2982

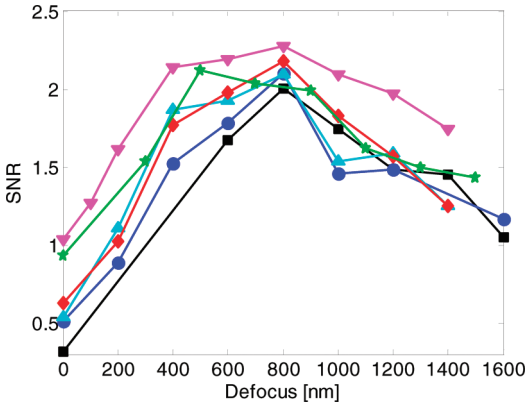


**Figure 9.** Signal-to-noise ratio (SNR) for various focal series, recorded at 20 $e^-/Å^2$ (pink and green curves) and 15 $e^-/Å^2$ (all other curves).

the surface ligands in the $Au_{102}(p\text{-MBA})_{44}$ structure, shown by well-defined electron density at 1.1 Å resolution, raised the possibility that exchange of the ligands for other sulfhydryl compounds would not readily occur. We therefore investigated the reactivity of $Au_{102}(p\text{-MBA})_{44}$ toward both a single chain antibody fragment bearing an exposed cysteine residue and a 14-residue oligodeoxyribonucleotide, modified with sulfhydryl group on a three-carbon linker at the 3′-end. The reaction proceeded rapidly to completion in both cases (Figure 6). Reaction with other proteins (AsdP-aspartate decarboxylase and Med31) was also observed (data not shown). Treatment of $Au_{102}(p\text{-MBA})_{44}$ with glutathione (repassivation) before the addition of protein abolished reactivity.

**Electron Microscopy (EM).** Purified $Au_{102}(p\text{-MBA})_{44}$ was adsorbed to polylysine-coated EM grids and imaged by transmission EM. Images of individual particles were analyzed by determination of the center of mass, rotational averaging, and thresholding with a MATLAB algorithm.[25] Such thresholding is arbitrary, and because the intensity of the projected image of a sphere is not a step function but rather decays from the center toward the edge (see below), the diameters of the particles may be underestimated in this way. Measurements on 2714 particles gave a mean diameter of 13.3 Å (Figure 7), and the standard deviation of the mean was 0.7 Å, indicative of a high degree of size homogeneity.

Our proposed use of gold nanoparticles as alignment markers for structure determination by cryo-EM[18] requires that the particles be individually visible in vitreous ice under low dose conditions, close to focus. To investigate $Au_{102}(p\text{-MBA})_{44}$ in this regard, we recorded images at a magnification of 80 000×, electron dose of 15−20 electrons/$Å^2$, and defocus values ranging from zero to 1600 nm under focus. The particles were readily observed, although their peak intensities were at most an order of magnitude above background. To better determine optimal imaging conditions, we computed average images of 200 individual particles at each defocus value (Figure 8A). We observed the expected variation of particle diameter, intensity, and Fresnel fringe around the particle image. Radial intensity distributions showed the peak intensity was highest at 800 nm under focus (Figure 8B). Comparison with the projected electron density, calculated from the structure of $Au_{102}(p\text{-MBA})_{44}$, showed good agreement in the range of 400−800 nm under focus, with the edge of the particle best defined at 400 nm (Figure 8C).

The visualization of particles for our proposed use in structure determination depends on the signal-to-noise ratio (SNR), defined as the intensity at the center of the image divided by the background noise. A series of measurements at two levels of electron dose showed the optimal signal-to-noise ratio was obtained at 800 nm under focus (Figure 9). Even under these imaging conditions, the signal-to-noise ratio was only 1.5−2, so $Au_{102}(p\text{-MBA})_{44}$ should be useful for structure determination by cryo-EM, but smaller particles may not.

## SUMMARY AND CONCLUSIONS

The first objective of this research was to improve the preparation of $Au_{102}(p\text{-MBA})_{44}$. Whereas the compound was previously obtained as a minor component of a mixture, the procedure reported here provides essentially pure material in good yield. Analysis by MS, TGA, XPS, and EM, which give values close to those calculated for $Au_{102}(p\text{-MBA})_{44}$, supports the near homogeneity of the material, while at the same time showing the validity of the methods for nanoparticle analysis. It remains to be determined whether small discrepancies between measured and calculated values reflect error in the measurements, limitations of the methods, or slight impurity of the material.

A second objective of the work was to assess the utility of $Au_{102}(p\text{-MBA})_{44}$ for structure determination by cryo-EM. The chief requirements are the conjugation of proteins, in particular single chain antibody fragments, at a level of one and only one per nanoparticle, and the visualization of individual nanoparticles under low dose conditions, close to focus. Both requirements were met, as $Au_{102}(p\text{-MBA})_{44}$ proved to be highly reactive toward sulfhydryl groups in proteins, and imaging conditions could be found for the detection of individual particles in cryo-EM.

## ASSOCIATED CONTENT

**Supporting Information.** A plot of absorbance versus concentration of the purified $Au_{102}$ preparation. This material is available free of charge via the Internet at http://pubs.acs.org.

## AUTHOR INFORMATION

**Corresponding Author**
kornberg@stanford.edu

## ACKNOWLEDGMENT

We thank Ming Lee Tang for help with TGA, Stephen Connor for help with near-IR measurements, and Ching-Mei Hsu for help with XPS. We are also grateful to Maia Azubel for advice and discussion. This research was supported by NSF grant CHE 0750059 to R.D.K.

## REFERENCES

(1) Brust, M.; Kiely, C. J. In *Colloids and Colloid Assemblies*; Caruso, F., Ed.; Wiley-VCH: Weinheim, Germany, 2004; pp 96−119.
(2) Daniel, M. C.; Astruc, D. *Chem. Rev.* **2004**, *104*, 293–346.
(3) Ackerson, C. J.; Jadzinsky, P. D.; Sexton, J. Z.; Bushnell, D. A.; Kornberg, R. D. *Bioconjugate Chem.* **2010**, *21*, 214–218.
(4) Jadzinsky, P. D.; Calero, G.; Ackerson, C. J.; Bushnell, D. A.; Kornberg, R. D. *Science* **2007**, *19*, 430–433.
(5) (a) Walter, M.; Akola, J.; Lopez-Acevedo, O.; Jadzinsky, P. D.; Calero, G.; Ackerson, C. J.; Whetten, R. L.; Grönbeck, H.; Häkkinen, H. *Proc. Natl. Acad. Sci. U.S.A.* **2008**, *105*, 9157–9162. (b) Häkkinen, H. *Chem. Soc. Rev.* **2008**, *37*, 1847–1859.
(6) Fields-Zinna, C. A.; Sampson, J. S.; Crowe, M. C.; Tracy, J. B.; Parker, J. F.; deNey, A. M.; Muddiman, D. C.; Murray, R. W. *J. Am. Chem. Soc.* **2009**, *131*, 13844–13851.

(7) Chaki, N. K.; Negishi, Y.; Tsunoyama, H.; Shichibu, Y.; Tsukuda, T. *J. Am. Chem. Soc.* **2008**, *130*, 8608–8610.
(8) Donkers, R. L.; Song, Y.; Murray, R. W. *Langmuir* **2004**, *20*, 4703–4707.
(9) Schaaff, T. G.; Knight, G.; Shafigullin, M. N.; Borkman, R. F.; Whetten, R. L. *J. Phys. Chem. B* **1998**, *102*, 10643–10646.
(10) Jimenez, V. L.; Georganopoulou, D. G.; White, R. J.; Harper, A. S.; Mills, A. J.; Lee, D.; Murray, R. W. *Langmuir* **2004**, *20*, 6864–6870.
(11) Hostetler, M. J.; Wingate, J. E.; Zhong, C.-J.; Harris, J. E.; Vachet, R. W.; Clark, M. R.; Londono, J. D.; Green, S. J.; Stokes, J. J.; Wignall, G. D.; Glish, G. L.; Porter, M. D.; Evans, N. D.; Murray, R. W. *Langmuir* **1998**, *14*, 17–30.
(12) Murray, R. W. *Chem. Rev.* **2008**, *108*, 2688–2720.
(13) Toikkanen, O.; Ruiz, V.; Ronnholm, G.; Kalkkinen, N.; Liljeroth, P.; Quinn, B. M. *J. Am. Chem. Soc.* **2008**, *130*, 11049–11055.
(14) Whetten, R. L.; Khoury, J. T.; Alvarez, M. M.; Murthy, S.; Vezmar, I.; Wang, Z. L.; Stephens, P. W.; Cleveland, C. L.; Luedtke, W. D.; Landman, U. *Adv. Mater.* **1996**, *8*, 428–433.
(15) Negishi, Y.; Nobusada, K.; Tsukuda, T. *J. Am. Chem. Soc.* **2005**, *127*, 5261–5270.
(16) Ackerson, C. J.; Sykes, M. T.; Kornberg, R. D. *Proc. Natl. Acad. Sci. U.S.A.* **2005**, *102*, 13383–13385.
(17) Ackerson, C. J.; Jadzinsky, P. D.; Jensen, G. J.; Kornberg, R. D. *J. Am. Chem. Soc.* **2006**, *128*, 2635–2640.
(18) Jensen, G. J.; Kornberg, R. D. *Proc. Natl. Acad. Sci. U.S.A.* **1998**, *95*, 9262–9267.
(19) Brust, M.; Fink, J.; Bethell, D.; Schiffrin, D. J.; Kiely, C. *J. Chem. Soc., Chem. Commun.* **1995**, 1655–1656.
(20) Alvarez, M. M.; Khoury, J. T.; Schaaff, T. G.; Shafigullin, M. N.; Vezmar, I.; Whetten, R. L. *J. Phys. Chem. B* **1997**, *101*, 3706–3712.
(21) Maye, M. M.; Han, L.; Kariuki, N. N.; Ly, N. K.; Chan, W. B.; Luo, J.; Zhong, C. J. *Anal. Chim. Acta* **2003**, *496*, 17–27.
(22) Rance, G. A.; March, D. H.; Khlobystov, A. N. *Chem. Phys. Lett.* **2008**, *460*, 230–236.
(23) Wuelfing, W. P.; Zamborini, F. P.; Templeton, A. C.; Wen, X.; Yoon, H.; Murray, R. W. *Chem. Mater.* **2001**, *13*, 87–95.
(24) Dass, A.; Guo, R.; Tracy, J. B.; Balasubramanian, R.; Douglas, A. D.; Murray, R. W. *Langmuir* **2008**, *24*, 310–315.
(25) Ackerson, C. J.; Jadzinsky, P. D.; Kornberg, R. D. *J .Am. Chem. Soc.* **2005**, *127*, 6550–6551.